Mesoscopic chemical heterogeneities in laser powder bed fused CoCrMo and Ni mixed powders and their effect on the mechanical properties

Siyuan Wei[1,2,*], Yakai Zhao[1,2], Baicheng Zhang[3], Pei Wang[2], Upadrasta Ramamurty[1,2]

[1]*School of Mechanical and Aerospace Engineering, Nanyang Technological University, Singapore 639798, Republic of Singapore.*

[2] *Institute of Materials Research and Engineering (IMRE), Agency for Science, Technology and Research (A*STAR) , 2 Fusionopolis Way, Innovis #08-03, Singapore 138634, Republic of Singapore.*

[3]*Advanced Material & Technology Institute, University of Science and Technology Beijing, Beijing, 100083, P.R. China*

*Corresponding author: wei_siyuan@imre.a-star.edu.sg

Abstract:

Microstructural heterogeneity is a feature of common occurrence in alloys additively manufactured using techniques such as laser powder bed fusion (LPBF). Additionally, chemical heterogeneities can arise both at micro- and meso-scales, especially when powder mixtures are used. While such chemical heterogeneities are considered undesirable hitherto, recent studies show that they may be beneficial in tailoring for the desired mechanical property combinations. In this study, we fabricated a graded alloy coupon with the mixed powders of the CoCrMo alloy and elemental Ni and investigated the microstructural and mesoscopic chemical heterogeneities in it. Chemical heterogeneities, which are either rich in Ni or CoCrMo, were observed due to the incomplete mixing of the powders. Banded patterns, with alternating layers that are enriched with different chemical species, were also observed. Distinct stacking fault energies between these chemical heterogeneities result in distinct deformation mechanisms; while planar slip and strain-induced martensitic transformation occur in the CoCrMo-rich heterogeneities, homogenous deformation associated with the wavy slip occurs in the Ni-rich ones. Detailed mechanical property characterizations show that the microscale chemical segregation not only strengthens the matrix but also improves the work hardening ability of the bulk material through kinematic hardening mechanism. These findings substantiate the key design principles for exploiting chemical segregations that form during *in situ* alloying for simultaneous enhancement of the strength and ductility in AM alloys.

Keywords: CoCrMo alloy; laser powder bed fusion; strengthening mechanism; heterogeneity;

nanoindentation.

1. Introduction

The microstructures of additively manufactured (AM) alloys using techniques such as the laser powder bed fusion (LPBF) are often heterogenous and hierarchical [1-4], which are increasingly being acknowledged as pathways to impart unique combinations of mechanical properties to the AM alloys [4]. Due to the fabrication freedom available in AM, i.e., flexible feedstock options and adjustable process parameters, it is further feasible to convert these serendipitous findings of heterogeneities into reliable design principles [5-7]. A particularly promising aspect is chemical heterogeneity, which inevitably occurs irrespective of the form of the powder feedstock, i.e., pre-alloyed or mixed. When using pre-alloyed powders, the chemical heterogeneity is typically limited to the inter-dendrite regions or the boundaries of the cellular structures (if present), due to the elemental partitioning at the liquid/solid interface during solidification [8,9]. On the other hand, mixing of two or more types of elemental or pre-alloyed powders can generate more pronounced (both in terms of the composition and length scale) chemical heterogeneity, due to the inadequate mixing of powders, size variations between powders, and the differences in the melting temperatures of the constituent components [4,10-12]. Hence, *in situ* alloying (using mixed powders) holds greater promises in the studies aiming at designing and modulating the chemical heterogeneity.

Until recently, the pursuit of both microstructurally and chemically homogeneous AM parts implicitly assumes that chemical heterogeneities are 'undesirable'. Therefore, additional processes or specific conditions are often mandated to avoid or mitigate heterogeneity. For example, the electrostatic assembly technique of zirconium on the pre-alloyed Al alloy powders was utilized to achieve homogenous mixture [13]. Similarly, a special combination of the fabrication parameters of high power and high speed top-hat laser was utilized to melt the refractory Nb powders (and in that process reduce the chemical inhomogeneity) during *in situ* alloying to fabricate a Ti-Nb alloy [14]. However, recent developments point to the fact that the chemical heterogeneities formed during the *in situ* alloying can be utilized to modulate the phase variations and, in the process, enhance the mechanical properties of the alloys [6,7,15]. For example, it was demonstrated that the heterogeneous clusters of α' and β phases in a hybrid Ti alloy can result in a combination of high strength, work hardening capability, and ductility [15]. By utilizing the discrete distribution of minor Ni powders, a new multiphase microstructures in a duplex steel in the as-fabricated condition is reported [7].

Inspired by the biological materials with spatial gradients in the local chemical compositions, chemical heterogeneity has been introduced into engineering materials to enhance the functional and mechanical properties [16,17]. In these studies, the spatial distribution, volume fraction, and morphology of the heterogeneous microstructures constituting hard and soft regions are found to play a significant role in affecting the generation of back-stress/kinematic hardening and therefore the mechanical properties of the bulk parts [18-20]. Nevertheless, current understanding on the chemical heterogeneity in the alloys produced using LPBF is constrained by the premise that the *in situ* alloying induced segregations are random in their distributions, leaving the modulation of it largely unexplored. Indeed, varying physical properties (e.g., melting point, thermal conductivity, and absorptivity of laser) and different characteristics of the powders (size, morphology, and flowability) can result in complex thermal history during *in situ* alloying and then relatively randomized micro- and meso-structures. *Prima facie,* chemical heterogeneities seem chaotic. For gaining insights into the role played by them, if any, on the mechanical behavior of the AM alloys, modulation of such heterogeneities at the meso-scale is essential. Such a knowledge could eventually enable the development of reliable and powerful design principles for broader classes of alloys.

Keeping the above issues in mind, in this study, we modulated the formation and distribution of chemical segregations via manipulating the duration available for powder mixing and scanning strategy. For this purpose, pre-alloyed Co29Cr6Mo and elemental Ni powders were chosen as an example system. The following are the reasons behind. (i) This combination of alloy powders can lead to the formation of a single FCC phase in the as-deposited state. (If more than one phase is present in the microstructure, it could complicate the deciphering of the chemical heterogeneity's role on the mechanical behavior.) (ii) The melting points of the both the powder constituents are similar [21,22]. This helps in avoiding cracking/delamination during the LPBF of the graded alloy. (iii) The distinct stacking fault energies (SFEs) [23,24] and mechanical properties (hardness) [25,26] of the two constituents can potentially highlight the contrast brought forth by the chemical heterogeneities. A continuous compositional gradient was created (Ni content varying from ~26.8 to 98.8 at.%) and chemical segregation into distinct bands was observed. The mechanism behind such band formation and the effect of the presence of such bands in the microstructure of the alloy on the local and overall mechanical behaviors are examined in detail and discussed.

2. Materials and Experiments

Commercially available powders of the alloy Co-29.4Cr-6Mo-0.8Si-0.75Mn-0.26Fe-0.15C (composition in wt.%), referred to simply as CoCrMo hereafter, and pure Ni, both spherical in shape and having diameters in the range of 13 to 53 μm, were used to fabricate the CoCrMo-Ni compositionally graded alloy (CGA). Figure 1 schematically illustrates the purpose-built LPBF system for fabricating the CGA with a continuous gradation. The powder deposition system in it comprises of the hopper, the mixer, and the re-coater [27,28]. A separator is placed along the diagonal of the powder hopper, which provides separate spaces for the feedstock CoCrMo and Ni powders, such that a lateral compositional gradation can be created. Underneath the feeding hopper, a mixer is utilized to mix the two component powders quickly before deposition on the substrate. A block with the size of 120 × 60 × 10 mm^3 (length, width, and height) was fabricated in an argon atmosphere by utilizing this setup. The following printing parameter combination was utilized: laser spot size = 35 μm, laser power w = 305 W, hatch spacing l = 90 μm, scan speed v = 960 mm/s, layer thickness t = 40 μm, and bi-directional scan strategy with a rotation (ϕ) of 67° between successive layers. This combination was arrived at after a prior process parameter optimization study, whose primary objective was to eliminate solidification cracking and minimize porosity (instead of trying to obtain homogeneous microstructure). The volumetric energy density ($J = w/lvt$) for the process parameter combination used is 88.3 J/mm^3. The fabricated CGA was sectioned at different positions along the gradient direction (GD), which is perpendicular to the build direction (BD), and then mechanically polished to mirror finish for the microstructural characterization. Optical microscope (OM) and scanning electron microscope (SEM, JEOL 7800F), equipped with an energy-dispersive X-ray spectroscope (EDS) and an electron backscatter diffraction (EBSD) detector, were utilized to study the chemical compositions, phases, and microstructures in the build (B-plane) and side (S-plane) planes of each sectioned specimen.

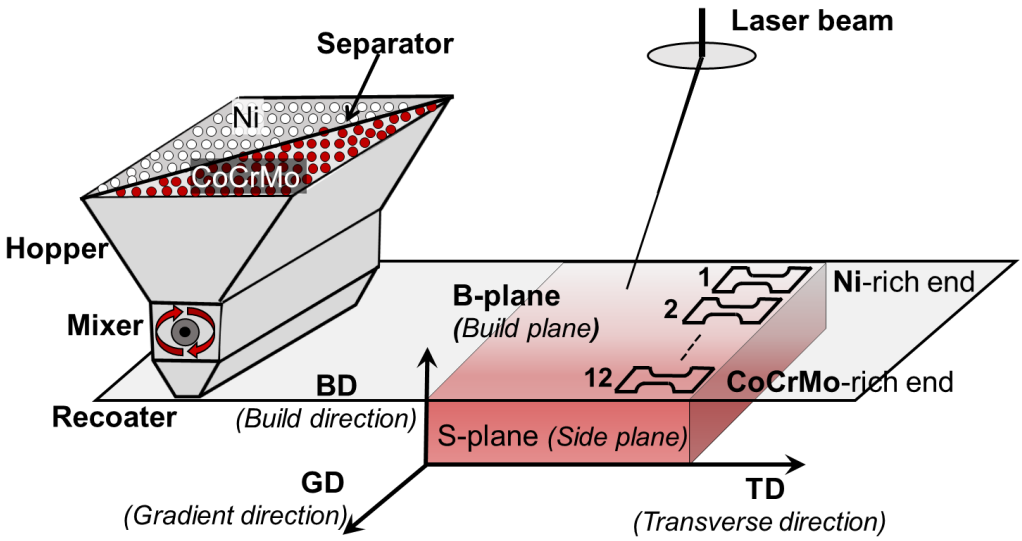

Figure 1. Schematic of the LPBF process employed in this study to fabricate samples with lateral compositional gradation.

Dog-bone-shaped tensile test specimens, whose gauge length, thickness, and width are 6, 1, and 2 mm, respectively, were extracted from 12 different equi-spaced locations of the fabricated CGA. Uniaxial tensile tests were performed (on five samples extracted from each region) at a nominal strain rate of 10^{-3} s^{-1} using an electro-mechanical tensile testing machine. Micro-scale hardness mapping (20 × 20 matrix, with 20 μm interspacing) using a Berkovich indenter was conducted using the Anton Paar MCT^3 Micro Combi Tester with a maximum load of 100 mN and loading/unloading rates of 200 mN/s. Micro-scratch tests were performed using the same instrument but with a Rockwell C indenter (spherical tip with 100 μm radius), a constant load of 1 N, and scratch speed of 66.7 μm/s over a total length of 10 mm. Before each scratch test, the profile of the surface to be scratched was measured. After the test, it was subtracted from the scratch profile, so as to ensure the measured penetration depth is not affected by the prior surface undulations (if any). In addition, nanoindentation hardness mapping (20 × 20 matrix, with 3.5 μm interspacing) was performed using a Bruker TI980 TriboIndenter equipped with Berkovich tip at a maximum load of 200 μN and loading/unloading rates of 500 μN/s.

3. Results

3.1. CoCrMo-Ni compositionally graded alloy

3.1.1 Chemical composition and microstructure

An EDS line scan made across GD of CGA is displayed in Figure S1 of the supplementary information (SI). It shows that a smooth compositional gradation is successfully created, with the Ni content varying from 98.8 to 26.8 at.% and the CoCrMo content complementing it (Co, as an indicator of CoCrMo alloys, varied from 0.7 to 46.6 at.%). To examine the variations in the chemical compositions along BD, EDS line scans were also performed along BD in each of the extracted samples. By assuming a normal distribution of the chemical composition, statistical analyses with the Kernel density estimates (KDEs) were performed to obtain the mean compositional values ($\bar{c}$), which are displayed in Figure 2(a) with the full width at half maximum (FWHM) represented as the error bars [29]. The full chemical compositions are listed in Table 1, and the designations of the samples are given. Examples of the KDEs of Co and Ni contents in the $(CoCrMo)_{2.7}Ni_{97.3}$, $(CoCrMo)_{44.3}Ni_{55.7}$, and $(CoCrMo)_{68.5}Ni_{31.5}$ samples are shown in Figure S2 of SI. It is seen that both the Ni and Co contents follow unimodal distributions in all the samples. Due to the local chemical heterogeneities formed during the *in situ* alloying process, significant FWHMs are noted in all of them. This observation is consistent with the significant compositional fluctuations observed in the plots of Co and Ni contents (Figure S1).

Table 1. Average chemical compositions and designation of samples.

Composition (at. %)	Designation (at. %)
$Co_{0.7}Cr_{0.4}Mo_{0.1}Ni_{98.8}$	$(CoCrMo)_{1.2}Ni_{98.8}$
$Co_{1.7}Cr_{0.8}Mo_{0.1}Ni_{97.3}$	$(CoCrMo)_{2.7}Ni_{97.3}$
$Co_{2.5}Cr_{1.3}Mo_{0.2}Ni_{96.0}$	$(CoCrMo)_{4.0}Ni_{96.0}$
$Co_{4.9}Cr_{2.5}Mo_{0.3}Ni_{92.2}$	$(CoCrMo)_{7.8}Ni_{92.2}$
$Co_{8.3}Cr_{4.3}Mo_{0.5}Ni_{86.9}$	$(CoCrMo)_{13.1}Ni_{86.9}$
$Co_{20.0}Cr_{10.3}Mo_{1.2}Ni_{68.5}$	$(CoCrMo)_{31.5}Ni_{68.5}$
$Co_{28.2}Cr_{14.4}Mo_{1.7}Ni_{55.7}$	$(CoCrMo)_{44.3}Ni_{55.7}$
$Co_{31.8}Cr_{16.3}Mo_{1.9}Ni_{50.0}$	$(CoCrMo)_{50.0}Ni_{50.0}$
$Co_{39.0}Cr_{19.9}Mo_{2.3}Ni_{38.8}$	$(CoCrMo)_{61.2}Ni_{38.8}$
$Co_{40.3}Cr_{20.6}Mo_{2.4}Ni_{36.7}$	$(CoCrMo)_{63.3}Ni_{36.7}$
$Co_{43.6}Cr_{22.3}Mo_{2.6}Ni_{31.5}$	$(CoCrMo)_{68.5}Ni_{31.5}$
$Co_{46.6}Cr_{23.9}Mo_{2.7}Ni_{26.8}$	$(CoCrMo)_{73.2}Ni_{26.8}$

To gain further insights into the nature of the local (or microscopic) chemical heterogeneities, EDS mapping was conducted. Representative Co and Ni maps obtained on the S-planes of the $(CoCrMo)_{2.7}Ni_{97.3}$, $(CoCrMo)_{44.3}Ni_{55.7}$, and $(CoCrMo)_{68.5}Ni_{31.5}$ samples are shown in Figures 2(b), 2(c), and 2(d), respectively. In these maps, localized microscopic areas, with ribbon-like appearance, enriched in either CoCrMo or Ni are observed. These are hereafter referred to as Co- and Ni-ribbons, respectively. In the samples where Ni is the predominant alloying element (i.e., samples $(CoCrMo)_{1.2}Ni_{98.8}$, $(CoCrMo)_{2.7}Ni_{97.3}$, and $(CoCrMo)_{4.0}Ni_{96.0}$), only Co-ribbons are observed. With an increasing Co (average Ni content $\leq$ 92.2 at.%), both Co- and Ni-ribbons are observed. In these samples, the ribbons appear to be arranged into homogeneous and heterogeneous bands; ribbons with chemical segregation are only observed in the latter.

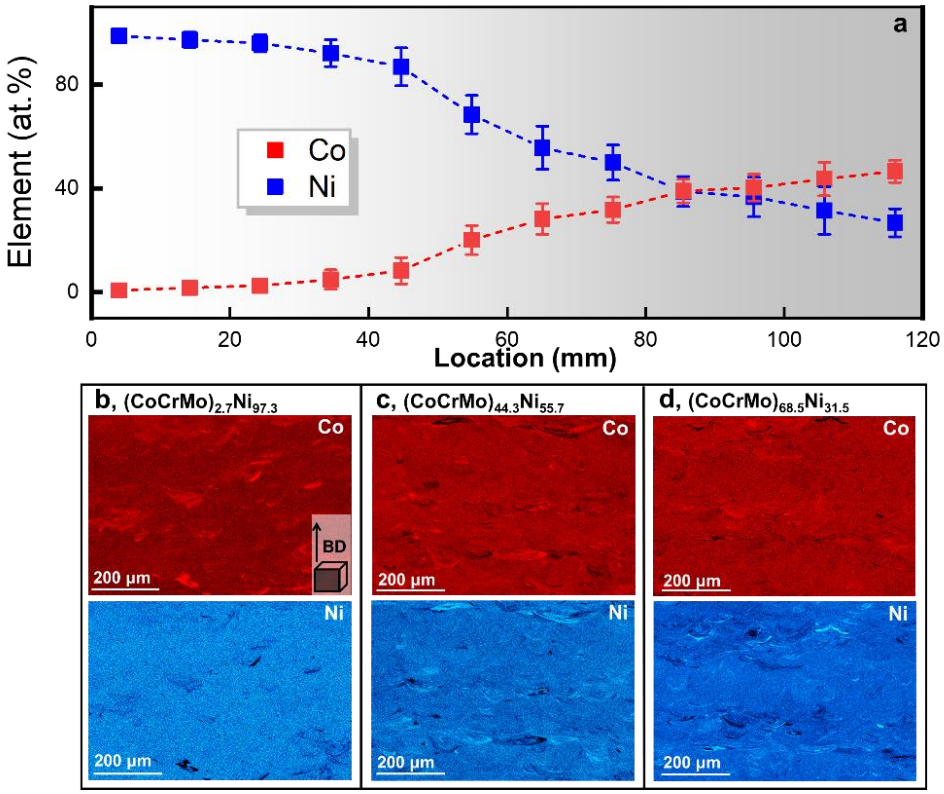

Figure 2. (a) Variations of the average values of the Ni and Co contents in the gauge areas of each of the 12 samples. Kernel density estimates (KDEs) methods were utilized to analyze the raw data and obtain the mean and full width at half maximum (FWHM) values; the latter are displayed as the error bars. (b–d) Representative localized inhomogeneities in the $(CoCrMo)_{2.7}Ni_{97.3}$, $(CoCrMo)_{44.3}Ni_{55.7}$, and $(CoCrMo)_{68.5}Ni_{31.5}$ samples, respectively.

The chemical composition (indicated by the Co content) and the area fractions of the Co- and Ni-ribbons are plotted against the average Ni content of each sample in Figure 3. (The area fractions are estimated in the following manner. The chemical compositions of the ribbons and taken from the EDS scan results on them. Then, the compositions that correspond to the ribbons are extracted from the extensive EDS line scan results.) As seen from Figure 3(a), the compositions of the ribbons are closely related to that of the matrix. From Figure 3(b), it is seen that the area fractions of Co- and Ni-ribbons in the samples with Ni content lower than 96 at.% remain nearly constant at 30 and 12%, respectively. In the $(CoCrMo)_{1.2}Ni_{98.8}$, $(CoCrMo)_{2.7}Ni_{97.3}$, and $(CoCrMo)_{4.0}Ni_{96.0}$ samples, approximately 25% Co-ribbons are found.

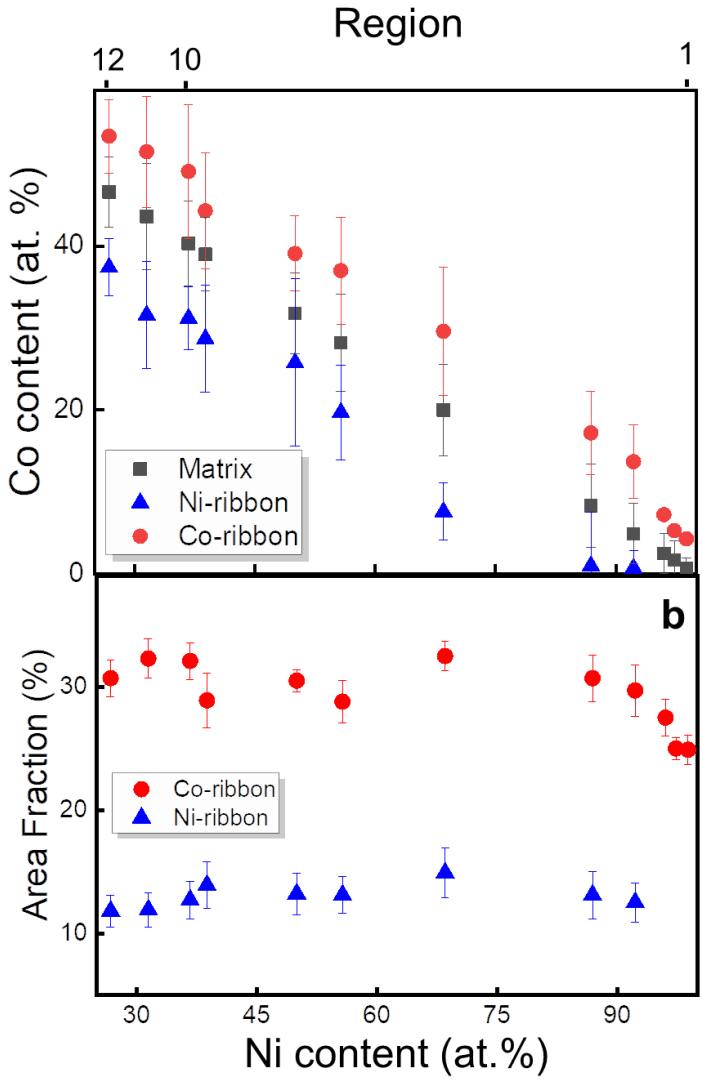

Figure 3. (a) Average Co contents of matrix, Co- and Ni-ribbons in all the 12 samples, plotted against the average Ni content in the sample. (b) Area fraction of Co- and Ni-ribbons**.**

Characterization on the etched S-planes across GD shows alternating layers of heterogeneous and homogeneous bands in samples with Ni content lower than 96 at.%. No evidence for banded chemical distribution could be found in the $(CoCrMo)_{1.2}Ni_{98.8}$, $(CoCrMo)_{2.7}Ni_{97.3}$, and $(CoCrMo)_{4.0}Ni_{96.0}$ samples, probably due to the limited amount of the CoCrMo powder addition. Representative OM images of the $(CoCrMo)_{2.7}Ni_{97.3}$, $(CoCrMo)_{44.3}Ni_{55.7}$, and $(CoCrMo)_{68.5}Ni_{31.5}$ samples are displayed in Figures 4(a), 4(b), and 4(c), respectively. The heterogeneous and homogeneous bands in them are marked by the red and blue blocks, respectively. The orientation maps (obtained using EBSD) of the areas marked by yellow dashed lines in Figures 4(a), 4(b), and 4(c) are shown in Figures 4(d), 4(e), and 4(f), respectively. Further analysis of the EBSD results revealed similar texture type (Figure 4(g)) and grain size (Figure 4(h)) across the compositional gradient. Above results show that the chemical heterogeneities do not significantly affect the size and morphology of the grains, i.e., there is no microstructural heterogeneity in the graded alloy. An example of the EBSD and EDS maps on both the S- and B-planes of the $(CoCrMo)_{68.5}Ni_{31.5}$ sample is shown in Figure S3.

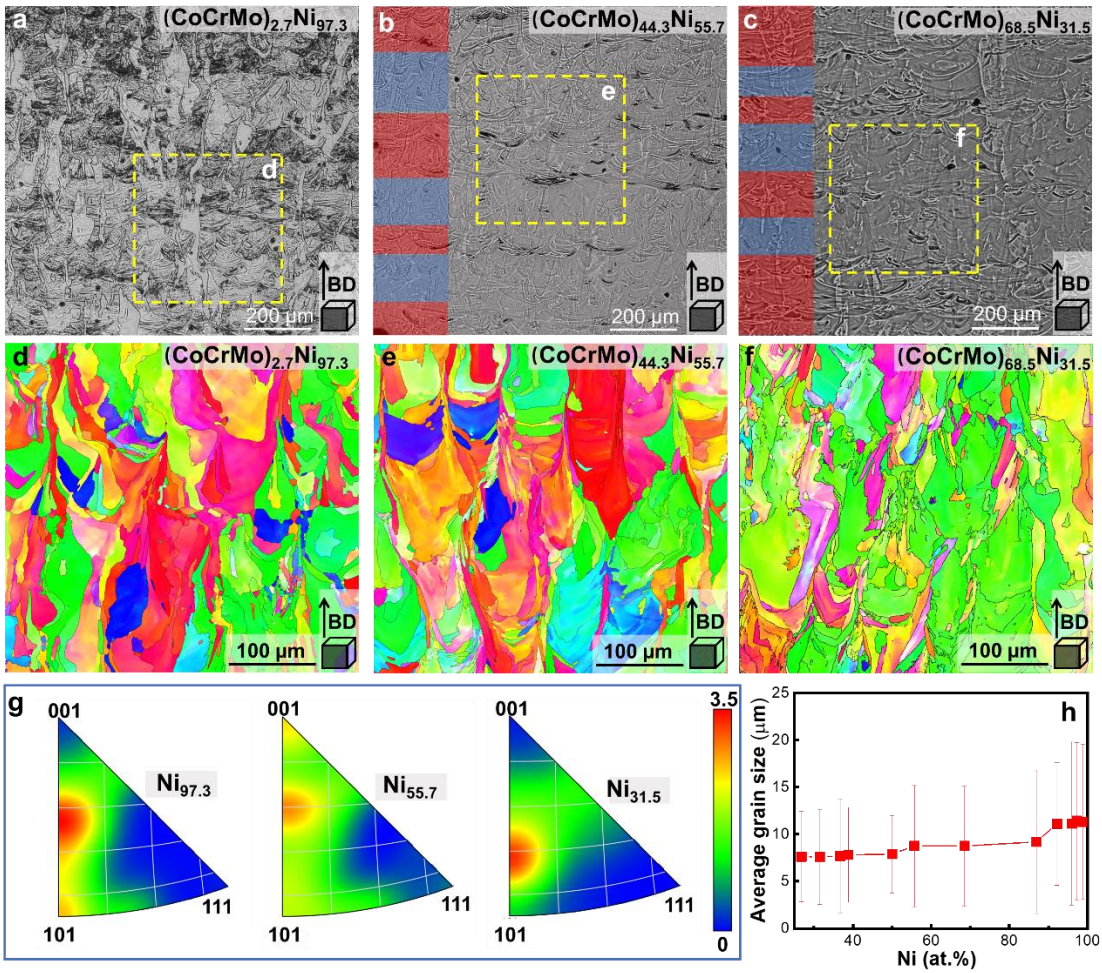

Figure 4. (a–c) Representative optical micrographs showing the chemical heterogeneities on the etched S-planes of the $(CoCrMo)_{2.7}Ni_{97.3}$, $(CoCrMo)_{44.3}Ni_{55.7}$, and $(CoCrMo)_{68.5}Ni_{31.5}$ samples, respectively. (d–f) Corresponding orientation maps obtained at areas marked by yellow dashed squares in (a–c), using electron backscatter diffraction (EBSD). (g) Inverse pole figures along BD. (h) Average grain sizes of each region obtained using EBSD.

3.1.2 Mechanical properties

Uniaxial tensile tests were performed on the samples extracted from 12 equi-spaced locations, and the representative engineering stress–engineering strain plots obtained on the $(CoCrMo)_{2.7}Ni_{97.3}$, $(CoCrMo)_{44.3}Ni_{55.7}$, $(CoCrMo)_{61.2}Ni_{38.8}$, $(CoCrMo)_{63.3}Ni_{36.7}$, and $(CoCrMo)_{68.5}Ni_{31.5}$ samples are shown in Figure 5(a). The variations in the instantaneous work hardening rates are plotted against the true plastic strain in Figure 5(b), and the yield strength (σ_y), ultimate tensile strength (σ_u), and strain to failure (ε_f) as a function of the Ni contents are displayed in Figures 5(c) and 5(d). The following are the key features that can be seen from Figure 5. (i) Both σ_y and σ_u depend on the chemical composition, such that they increase almost linearly as the Ni content decreases from 98.8 to 38.8 at.%. However, in the $(CoCrMo)_{63.3}Ni_{36.7}$, $(CoCrMo)_{68.5}Ni_{31.5}$, and $(CoCrMo)_{73.2}Ni_{26.8}$ samples, σ_y and σ_u remain

nearly invariant. (ii) A first order estimate of the work hardening ability of each alloy is made using the parameter $\Theta = (\sigma_u - \sigma_y)/\sigma_y$. From its variation with the Ni content displayed in Figure 5(c), two distinct groupings in Θ, on either side of Ni content = 38.8 at.%, can be noted, wherein the samples within each group have rather similar Θ values. An abrupt jump in Θ is seen between these two groups, as highlighted in Figure 5(c). (iii) The tensile stress-strain responses obtained from every sample that was tensile tested show continuously decreasing instantaneous work hardening rate (Figure 5(b)), indicating that the dislocation mediated plastic deformation governs the flow in all of them [30,31]. (iv) The average values of ε_f of all the 12 samples are above 20%, where the two end regions show higher ε_f than those in the middle of the CGA. This could be due to the differences in relative densities (ρ) as shown in Figure 5(d), where higher level of porosity is found in the middle regions.

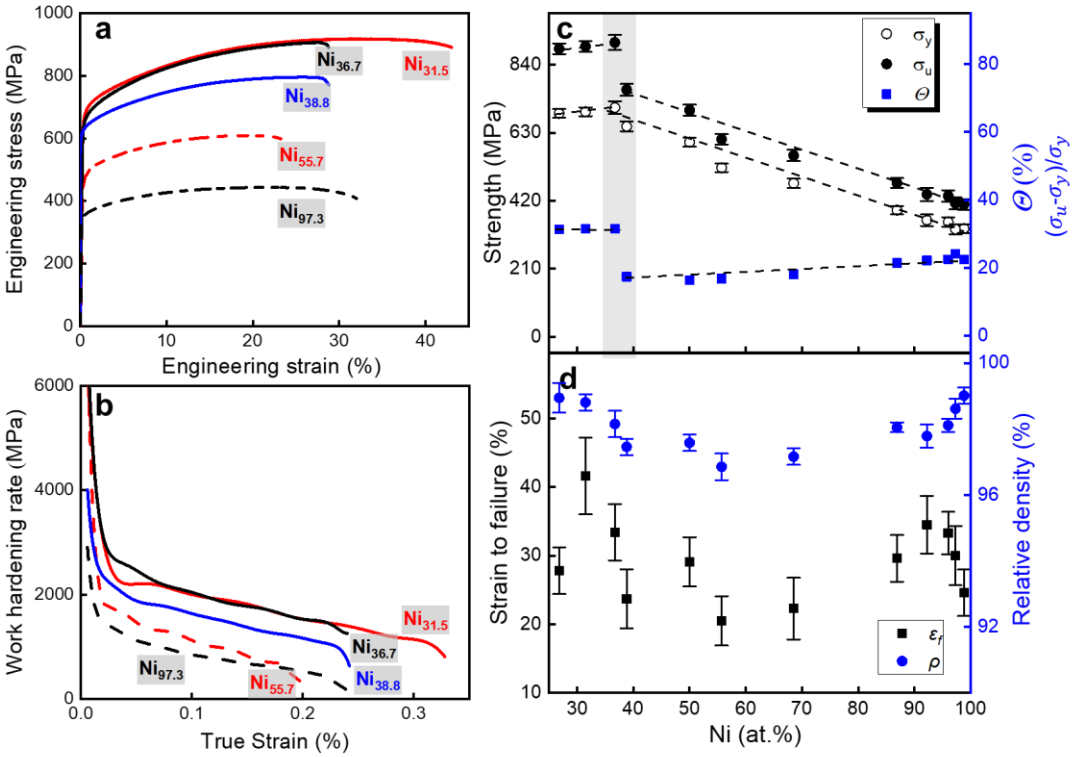

Figure 5. (a) Representative engineering stress-engineering strain plots of the $(CoCrMo)_{2.7}Ni_{97.3}$, $(CoCrMo)_{44.3}Ni_{55.7}$, $(CoCrMo)_{61.2}Ni_{38.8}$, $(CoCrMo)_{63.3}Ni_{36.7}$, and $(CoCrMo)_{68.5}Ni_{31.5}$ samples obtained from uniaxial tension. (b) Plot of instantaneous work hardening rate against the true strain. (c) The yield strength (σ_y), ultimate tensile strength (σ_u), and strain hardening ability (Θ) of different regions as a function of the Ni content in them. (d) Variations in the strain to failure (ε_f) and relative density (ρ) as a function of the Ni content.

3.2. Mechanical characterization of the banded mesostructure

The effect of the chemical distribution into bands on the mechanical behavior is characterized using both the micro- and nano-indentation techniques. An example of the micro-indentation mapping on the $(CoCrMo)_{68.5}Ni_{31.5}$ sample is shown in Figures 6(a); another one for the $CoCrMo)_{44.3}Ni_{55.7}$ sample is displayed in Figure S4. The microhardness maps cover two heterogeneous bands (located at the top and bottom of the mapped area) and one homogeneous band (middle of the mapped area), demarcated by the white dashed lines. The average microhardness of the whole mapped area is 2.6 ± 0.4 GPa. As seen in the microhardness map (Figure 6(b)) and the corresponding Co and Ni EDS maps (Figures 6(c) and 6(d)), the Co-ribbons have a higher average microhardness than the rest of the area examined. Note that no perceptible effect of the Ni-ribbons on the microhardness could be seen, possibly because of the comparatively large interspacing of the indents (~20 μm). The average microhardness of the 'heterogeneous band' is higher than that of the 'homogeneous band', probably due to the strengthening effect from the Co-ribbons.

Nanoindentation offers higher spatial resolution thanks to the small interspacing (~3.5 μm) that it permits. It was, therefore, utilized to further examine the effects of the Co- and Ni-ribbons on the nanohardness of local areas. An area with a Co-ribbon was intentionally selected for the nanohardness mapping. From Figures 6(e), 6(f), 6(g), and 6(h), it is clear that the nanohardness values are closely related to the relative chemical composition. The Co-ribbon shows a higher nanohardness of ~6.5 GPa compared to that of the matrix (~4.5 GPa), whereas the Ni-ribbon (e.g., left bottom of Figures 6(f), 6(g), and 6(h)) exhibits a lower nanohardness of ~3.5 GPa. Note that the hardness values obtained with the nanoindentation are higher than those obtained with the micro-indentation due to the indentation size effect [32].

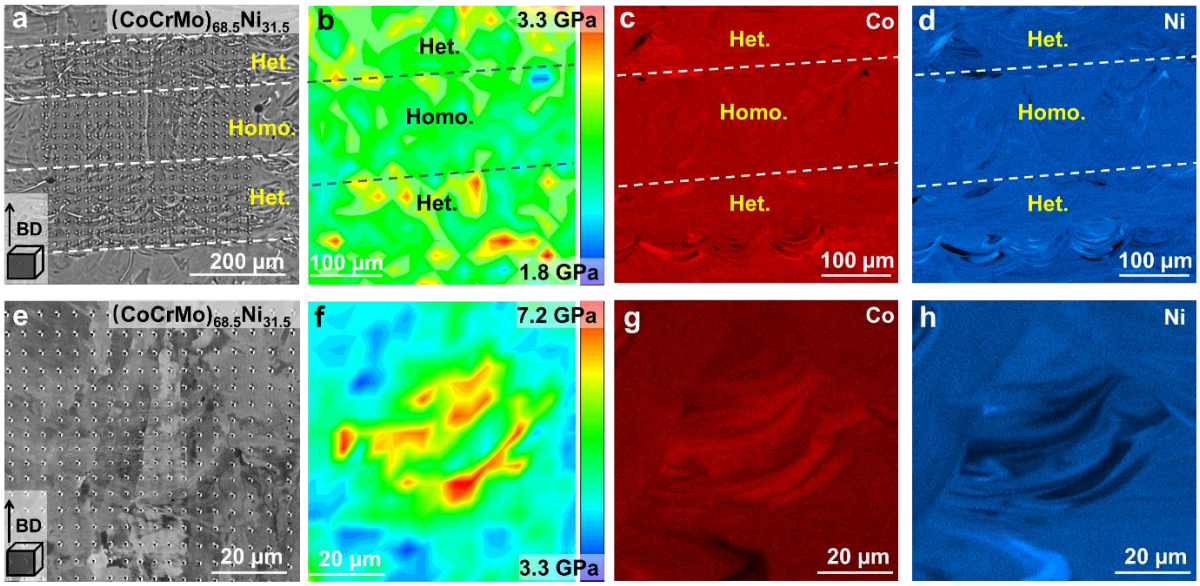

Figure 6. Optical images of the indents, hardness, and EDS mappings of the $(CoCrMo)_{68.5}Ni_{31.5}$ sample on its S-plane, obtained using micro-indentation (a–d) and nanoindentation mapping (e–h). Dashed lines in (a–d) indicate the boundaries of heterogeneous and homogenous bands.

To understand the fractions and length scales of these mesostructures more comprehensively and quantitatively, micro-scratch tests were conducted on each sample. As shown in Figure 7, which is a representative image obtained from the $(CoCrMo)_{68.5}Ni_{31.5}$ sample, a constant load of 1 N was utilized to scratch the S-plane over a length of 1 mm, which spans several heterogeneous and homogeneous bands (Figure 7(a)). The penetration depth (d) of the indenter during scratch test, which is an indicator of the local hardness, is plotted as a function of the distance (from the starting point of the scratch) in Figure 7(b). Note that a higher d indicates lower hardness, and *vice versa*. While d remains relatively constant in the homogeneous bands, it fluctuates significantly in the heterogeneous bands. Further EDS line scanning along the center of the scratch line (results shown in Figure 7(c)) reveals that chemical variation across the scratched length corresponds well with d: (i) areas that are rich in Ni (and hence poor in Co) have higher d, and *vice versa*; (ii) heterogeneous bands show evident serrations in composition, while homogeneous bands are relatively smoother in terms of the compositional variations.

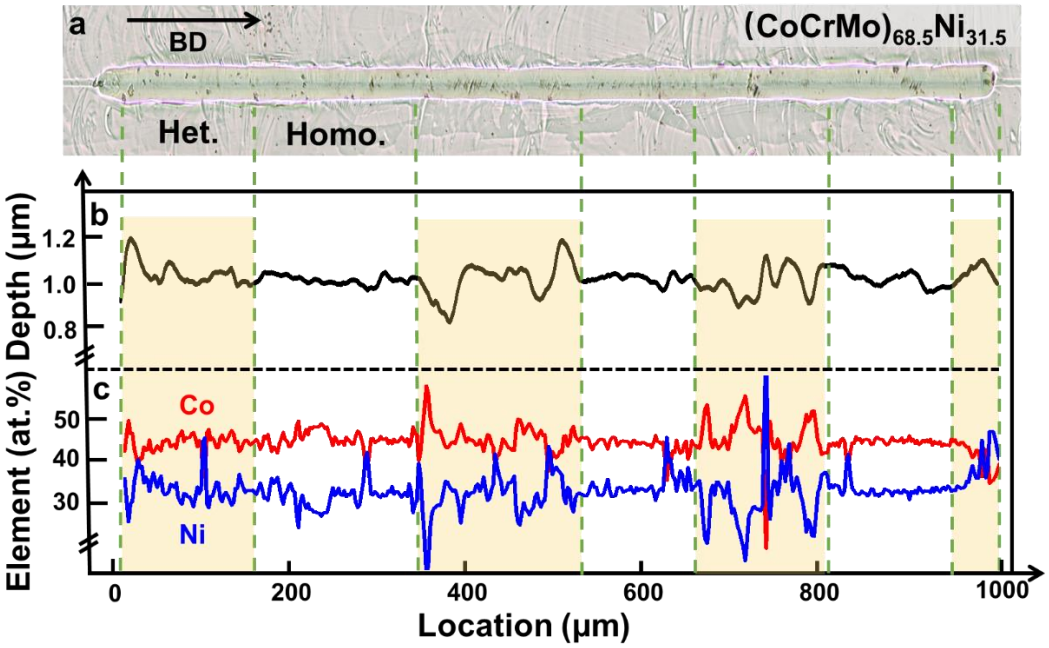

Figure 7. (a) Optical micrograph of micro-scratch test on the banded sample. (b) Resulting plot of penetration depth against location from scratch testing in (a). (c) Corresponding plots of Co and Ni compositions against location, obtained using EDS line scanning.

We utilized the same method for each sample obtained from different regions of the graded alloy coupon over a larger scratch distance of ~10 mm and analyzed the data of *d* obtained in terms of a probability density function (PDF) plots. Such plots for the $(CoCrMo)_{2.7}Ni_{97.3}$, $(CoCrMo)_{44.3}Ni_{55.7}$, $(CoCrMo)_{61.2}Ni_{38.8}$, and $(CoCrMo)_{68.5}Ni_{31.5}$ samples are shown as representative ones in Figure 8. It is clear from these plots that the distributions in *d* are, in most cases, bi- or multi-modal. Assuming that the underlying distributions for all the peaks are Gaussian, the PDF plots are deconvoluted, as shown. The key observations from them are the following. (i) In the samples with Ni content ≥ 96 at.%, the PDFs indicate to a predominantly unimodal distribution (see for example Figure 8(a)). (ii) Upon increasing the Co content (from samples $(CoCrMo)_{7.8}Ni_{92.2}$ to $(CoCrMo)_{61.2}Ni_{38.8}$), the distribution in *d* becomes bimodal (Figures 8(b) and 8(c)). (iii) In the samples $(CoCrMo)_{63.3}Ni_{36.7}$, $(CoCrMo)_{68.5}Ni_{31.5}$, and $(CoCrMo)_{73.2}Ni_{26.8}$, the PDF plots follow a trimodal distribution (Figure 8(d)).

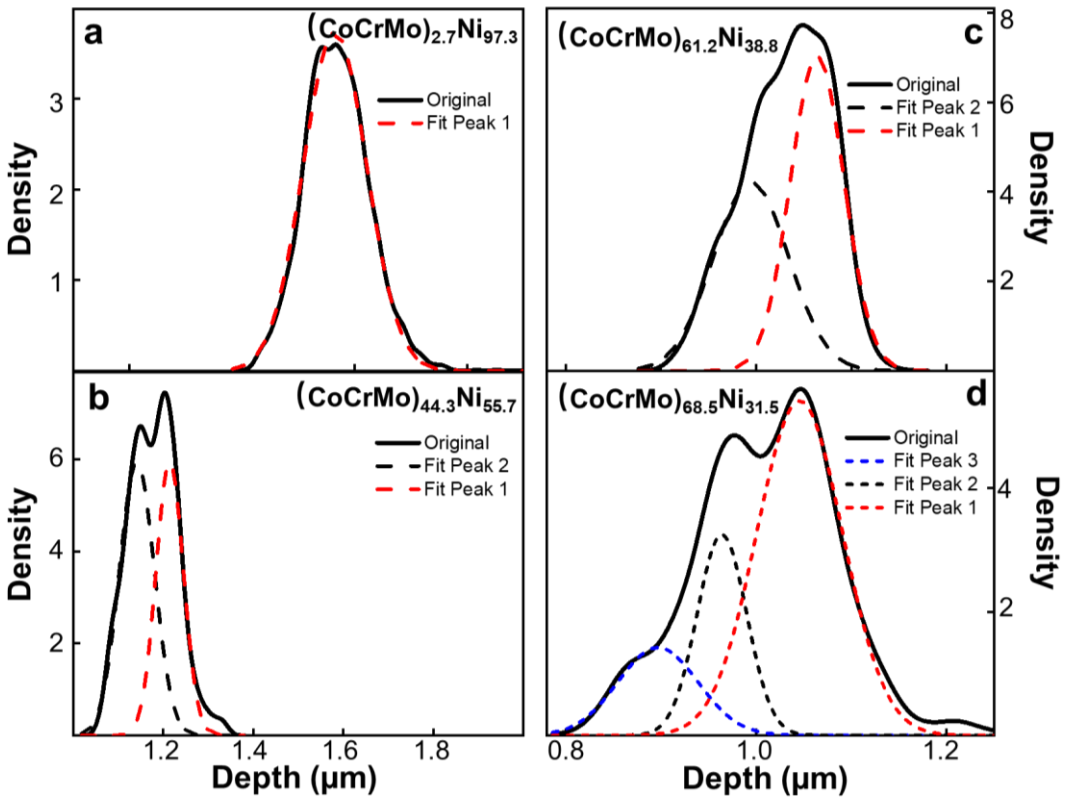

Figure 8. Probability density function (PDF) of penetration depth on S-plane of samples $(CoCrMo)_{2.7}Ni_{97.3}$, $(CoCrMo)_{44.3}Ni_{55.7}$, $(CoCrMo)_{61.2}Ni_{38.8}$, and $(CoCrMo)_{68.5}Ni_{31.5}$ obtained using scratch testing. Dashed lines are the fit peaks obtained via deconvolution of the PDF plots.

Variations in the reciprocal of the mean penetration depth, $1/\bar{d}$, which can be used as an indicator of the relative hardness, and the proportion of each deconvoluted peak of the PDF plots with the Ni content are shown in Figure 9. While the values of $1/\bar{d}$ corresponding to the peak 1 are the lowest in each region, they are the highest for peaks 3 (when present). Further observations are the following. (i) The hardness increases monotonically with a decrease in the Ni content from 98.8 to 36.7 at.%. Upon reaching a peak in the $(CoCrMo)_{63.3}Ni_{36.7}$ sample, hardness reduces as the Ni content decreases from 36.7 to 26.8 at.%. (ii) Except for the samples with 98.8–96.0 at.% Ni, where only one peak is present, the fraction of the soft peak 1 and hard peak 2 (or peaks 2 + 3) remain approximately constant at ~60% and 40%, respectively. (iii) Peak 3 in the $(CoCrMo)_{63.3}Ni_{36.7}$ sample shows higher hardness yet lower fraction than those in the $(CoCrMo)_{68.5}Ni_{31.5}$ or the $(CoCrMo)_{73.2}Ni_{26.8}$ samples.

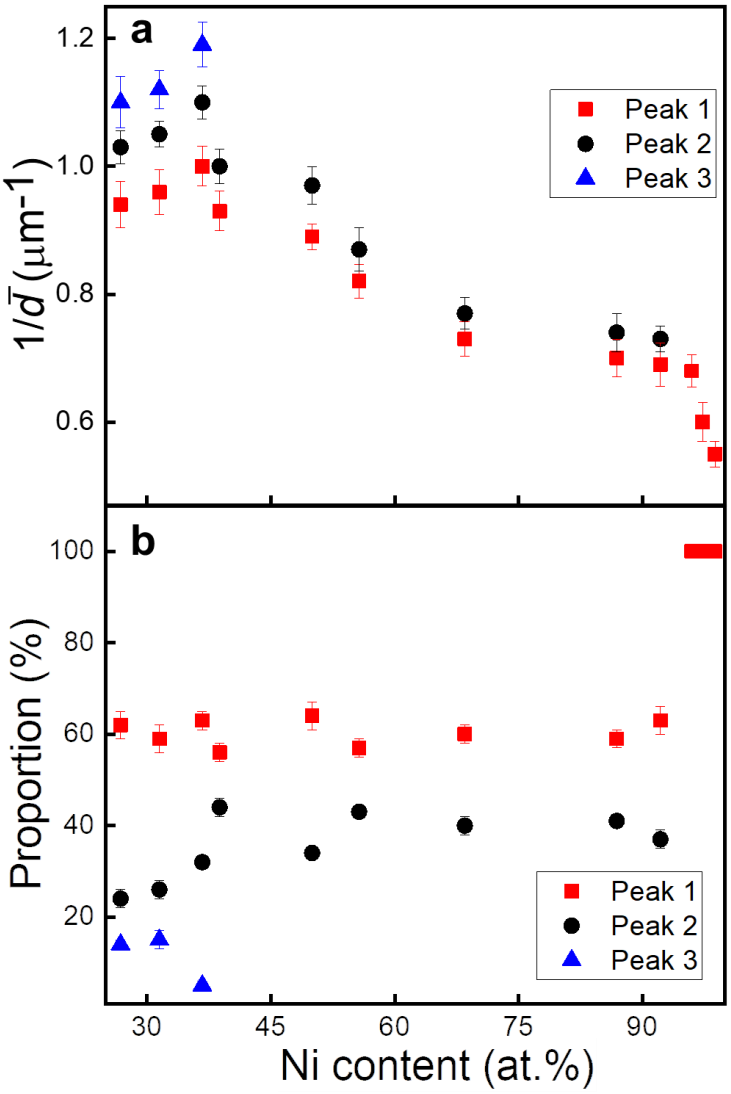

Figure 9. Plots of (a) $1/\bar{d}$ (the reciprocal of mean penetration depth) and (b) proportion of each peak obtained from probability density function plot in each region.

4. Discussion

Results of the microstructural characterization presented above establish that the *in situ* alloying that occurs during CGA fabrication leads to the formation of mesoscopic chemical segregation bands in the graded alloy (except at the Ni-rich end regions). Such a banded structure highlights the possibility of modulating chemical segregation into organized structures, in contrast to their seemingly randomized nature (as reported in some recent literature [6,15]). We believe that the banded structure initiates from the consistent scanning strategy across the entire area of the printed parts, which can retain the layer-by-layer

characteristics of the LPBF process. In the following section, the formation mechanism of the chemical heterogeneities and their effect on the mechanical properties are discussed.

4.1. Chemical segregation into mesoscopic bands

When the alloy constituents (components) have good solid solubility with each other and have similar melting points (which is the case here), the length scale of the chemical heterogeneities, and their degree of segregation within the alloy parts manufactured using LPBF largely depend on the nature of the powder feedstock, i.e., whether pre-alloyed powders, or well-mixed multiple types of powders, or mixed powders with initial clusters of segregation are used. (i) When pre-alloyed powders are used, the chemical segregation is induced by elemental partitioning at the liquid/solid interface upon solidification and is typically confined to the boundaries of the dendrite/cellular structures with limited amplitude [1,8,33]. For example, the chemical segregations at the cell boundaries of the LPBF 316L austenitic stainless steel are ~4 wt.% Cr and 1–3 wt.% Mn/Mo [9]. Depending on the size of cellular structures, these chemical heterogeneities are typically at the submicron scale [34]. (ii) Macroscale chemical homogeneity can also result from *in situ* alloying, when the powders are well mixed and the elements are miscible with each other [7,35,36]. Chemical segregation during *in situ* alloying is then induced by the different number of minor constituent's particles captured by the melt pools [7]. Here, chemical heterogeneity occurs at the inter-melt pool level, while each melt pool is considered homogeneous. The length scale in this case is controlled by melt pool size and the degree of overlap between adjacent melt pools. The amplitude of segregation in this scenario is found to be rather limited (less than ~5% [7]). (iii) A prior existence of powder clusters, induced by insufficient powder mixing, can lead to a marked chemical segregation during the LPBF process [37]. In this work, the powder mixing was limited by the short time span the powders spend in the mixer. As a result, microscale chemical heterogeneity is seen throughout the graded alloy (Figure 2). As it originates from the powder clusters, the length scales of such a chemical heterogeneity are affected by—but not confined to—the melt pool. Their shapes result from the combined effects of the recoil pressure, Marangoni force, surface tension, melt pool shape, and diffusion [38]. Due to such complex, inter-dependent, and collective effects, the shapes and sizes of the Co- and Ni-ribbons observed in the present work are irregular. More in-depth experimental and simulation work is required for a clearer understanding of their development (and how to best

control them). Here, we can only observe that most of the ribbons resemble the shape of the melt pool.

Consequently, the chemical segregation in the present case is significantly affected by the melt pool characteristics. Its distribution would follow the moving melt pool and thus laser scan track [38]. Under such scenario, the morphology/distribution of the segregation depends on the angle between the scanning and viewing directions. More specifically, when viewed along the scanning direction, only the ends of the scan tracks are visible and thus a limited number of ribbons can be seen. When the viewing direction is perpendicular to the scanning tracks, on the contrary, the side surfaces of the scan tracks are exposed so that more Co/Ni-ribbons are observed. In this work, the heterogeneous and homogeneous bands appear to contain different amounts of Co- and Ni-ribbons on the S-plane, but this is only an artefact that results from a change in the viewing orientation. Note that 67º is utilized in this work because it is a prime number, which minimizes the overlap of the scan tracks and thus facilitates homogeneity of the thermal history. One can imagine that rotation angles that favor overlapping of scan tracks, e.g., 0º and 90º, would result in microstructures strongly confined by the scale of the scan tracks, instead of banded patterns, as reported in the literature [39,40]. Other scan rotation angles could also result in the banded pattern; this is a highly promising aspect that needs to be further investigated in the future.

4.2. Effect of heterogeneities on the mechanical behaviors

The superior strength and ductility combination that is often observed in the mechanical response of heterogeneous materials, with laminated [41], gradient [42], and duplex phase [43] microstructures, where both soft and hard domains coexist, is often rationalized by recourse to the back-stress mediated kinematic strain hardening [19,44,45]. During the plastic deformation of these heterogeneous materials, the strain would be inhomogeneous but continuous, which produces strain gradients that are accommodated by geometrically necessary dislocations (GNDs) [18,20]. Upon the partitioning of plastic strain between hard and soft domains, GNDs piled up against the interdomain interfaces would produce a back stress in the soft domain in a direction opposite to the applied shear stress, and a forward stress in the hard domain in the same direction of the applied stress [18]. To examine if such mechanism exists in the current context, we tensile strained (by 10% total) well-polished samples, which were extracted from the regions with the average chemical compositions of $(CoCrMo)_{61.2}Ni_{38.8}$ and $(CoCrMo)_{68.5}Ni_{31.5}$, before examining them. The observed slip traces

(using SEM) along with the chemical compositions (evaluated with the aid of SEM-EDS) are shown in Figures S5 and 10, respectively. It is observed that the slip traces in the Co-ribbons are deep with large spacing, while densely spaced, but shallow, slip traces are seen in the matrix and Ni-ribbons. These distinct morphologies of the slip traces in the Co- and Ni-rich ribbons can be attributed to the variation of the stacking fault energy (SFE) between them. As is well known, a low SFE leads to high slip planarity whereas a high SFE fosters cross-slip of screw dislocations and hence 'homogenization' of plasticity at the microscopic scale ('wavy slip') [46,47]. While Ni has high SFE (~150–300 mJ/m^2 [48,49]), the FCC CoCrMo alloy is considered to have negative SFE [23]. This is because the additions of both Cr and Mo as solutes would decrease SFE of pure Co (~0 mJ/m^2 [23,50]) to the negative territory [50]. When SFE is negative, the dissociation of a full dislocation into two widely separated partials is energetically favored. Due to the dominance of planar slip and the glide of larger number of dislocations on relatively fewer slip planes, the slip traces in the Co-ribbon are widely separated but with larger offsets as compared to those of the Ni-ribbon and the matrix. Note that, although the composition of the matrix and ribbons were obtained (Figure 3), the exact values of their SFE were not determined. The SFE of alloys can be reliably established through molecular dynamics (MD) or density function theory (DFT) simulations [50,51]. However, studying the SFE of quaternary Co alloys is highly complicated and beyond the scope of this work, especially with the presence of chemical heterogeneity. Furthermore, discussing the SFE qualitatively, on the basis that higher Co content leads to lower SFE, is sufficient to explain the phenomena here.

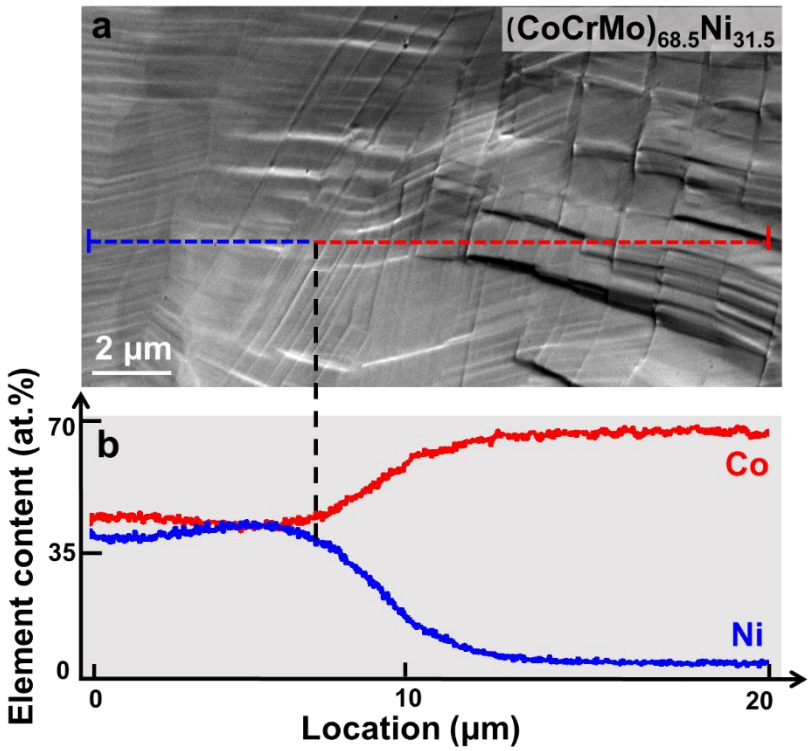

Figure 10. Morphologies of slip traces (a) on sample $(CoCrMo)_{68.5}Ni_{31.5}$ with the corresponding EDS line scan results (b).

The relative difference in the hardness of the hard and soft domains, viz. Co-ribbon/matrix, Co-ribbon/Ni-ribbon, and matrix/Ni-ribbon, also plays a significant role in affecting the build-up of back and forward stresses. (i) When the hardness difference between the hard and soft domains is large, their boundaries would be effective in resisting the dislocation glide. Hence, the plastic deformation in the hard domain can only initiate when the back stress in the soft domain becomes high enough to facilitate continuous deformation in both the domains. This, in turn, would enhance the work hardening in the alloy [18]. (ii) When the hardness difference is not substantial, the plastic deformation in the hard domain can be activated by either the leading dislocation being 'pushed' into the hard domain or dislocation emission from the domain boundary. The resulting back and forward stresses in this case would be limited [18]. This background information will be utilized in the context of rationalizing the observed mechanical property variations across the graded alloy, as following.

In Figure 5, a trend of increasing strength with an increase in the overall Co content in the alloy (or conversely, with a decreasing Ni content) is seen. This is expected, as the CoCrMo alloy has higher strength than pure Ni [25,52]. While a linear relationship between

σ_y (as well as σ_{UTS}) and the Ni contents from $(CoCrMo)_{1.2}Ni_{98.8}$ to $(CoCrMo)_{61.2}Ni_{38.8}$ is indeed noted in Figure 5(b), an abrupt increase in σ_{UTS} and work hardening ability is observed in the alloys with the $(CoCrMo)_{63.3}Ni_{36.7,}$ $(CoCrMo)_{68.5}Ni_{31.5}$, and $(CoCrMo)_{73.2}Ni_{26.8}$ compositions, while σ_y appears to be within the scatter band of the otherwise linear increase. The enhanced work hardening in $(CoCrMo)_{63.3}Ni_{36.7,}$ $(CoCrMo)_{68.5}Ni_{31.5}$, and $(CoCrMo)_{73.2}Ni_{26.8}$ can be attributed to the appearance of the hard peak 3 from the analysis of micro-scratch testing (Figures 8 and 9).

In samples with the Ni content ≥ 96 at.%, the observed unimodal distribution of *d* (Figure 8(a)) indicates relatively uniform hardness. From the regions in which the Ni content varies between 92.2 to 28.8 at.%, *d* is bimodal due to the hardening caused by the Co-ribbons in the heterogeneous band, as evidenced by the hardness maps displayed in Figures 6 and S4. To study the formation mechanism of peak 3 in the deconvoluted distribution of *d* in the regions with Ni less than 36.7 at.%, EBSD images obtained on the 10% pre-strained samples of $(CoCrMo)_{68.5}Ni_{31.5}$ and $(CoCrMo)_{61.2}Ni_{38.8}$ were compared in Figure 11. The latter region shows the same FCC phase before and after plastic deformation, i.e., no stress induced phase transformation takes place in it. In the deformed $(CoCrMo)_{68.5}Ni_{31.5}$, in contrast, minor quantities (5.1%) of a hexagonal close packed (HCP) phase were observed. Further EBSD characterization of the same alloy, $(CoCrMo)_{68.5}Ni_{31.5}$, which was subjected to only a 5% pre-strain (in Figure S6), shows no sign of such a phase. On this basis, we surmise that the observed HCP phase is possibly a result of strain-induced martensitic transformation [53].

In the CoCrMo alloy, the ε-HCP phase is thermodynamically more stable than the γ-FCC phase [54] due to the fact that the negative SFE would favor the motion of isolated Shockley partials over the paired motion of the leading and trailing Shockley partials [53]. Since Ni is a strong FCC stabilizer and possesses high SFE [55], its addition to the CoCrMo alloy stabilizes the FCC phase. Consequently, a single FCC phase is observed across the entire compositionally graded alloy that was examine in this study. However, due to the formation of the Co-rich ribbons, some local areas can still have negative SFE, which makes the FCC phase in them metastable. When such a sample is deformed to a critical strain, the metastable γ-FCC phase can undergo martensitic transformation to ε-HCP [53], which can contribute to additional work hardening of the alloy [56]. With an increasing Co content in the compositionally graded samples, the SFE of certain regions of the Co-rich ribbons in $(CoCrMo)_{63.3}Ni_{36.7,}$ $(CoCrMo)_{68.5}Ni_{31.5}$, and $(CoCrMo)_{73.2}Ni_{26.8}$ can reach critical values that favor the strain-induced martensitic transformation, which accounts for the enhanced work

hardening ability observed in the tensile coupons extracted from those samples (Figure 5). Post-mortem EBSD characterization (Figure S7) on the samples after scratch testing also shows a combination of HCP and FCC phases in $(CoCrMo)_{63.3}Ni_{36.7}$, $(CoCrMo)_{68.5}Ni_{31.5}$, and $(CoCrMo)_{73.2}Ni_{26.8}$, with HCP phase fractions of 1.5%, 3.8%, and 3.6%, respectively. The fraction of HCP phase was determined using the following method. The scratched areas were first extracted from the original EBSD mapping, such that the total numbers of pixels within the testing areas can be obtained. Subsequently, the HCP phase fraction was calculated by dividing the number of pixels in the HCP phase by the total number of pixels in the scratched areas. Only FCC phase was seen in the rest of the samples. This observation confirms that the peak 3 in Figure 8 is closely related to martensitic transformation.

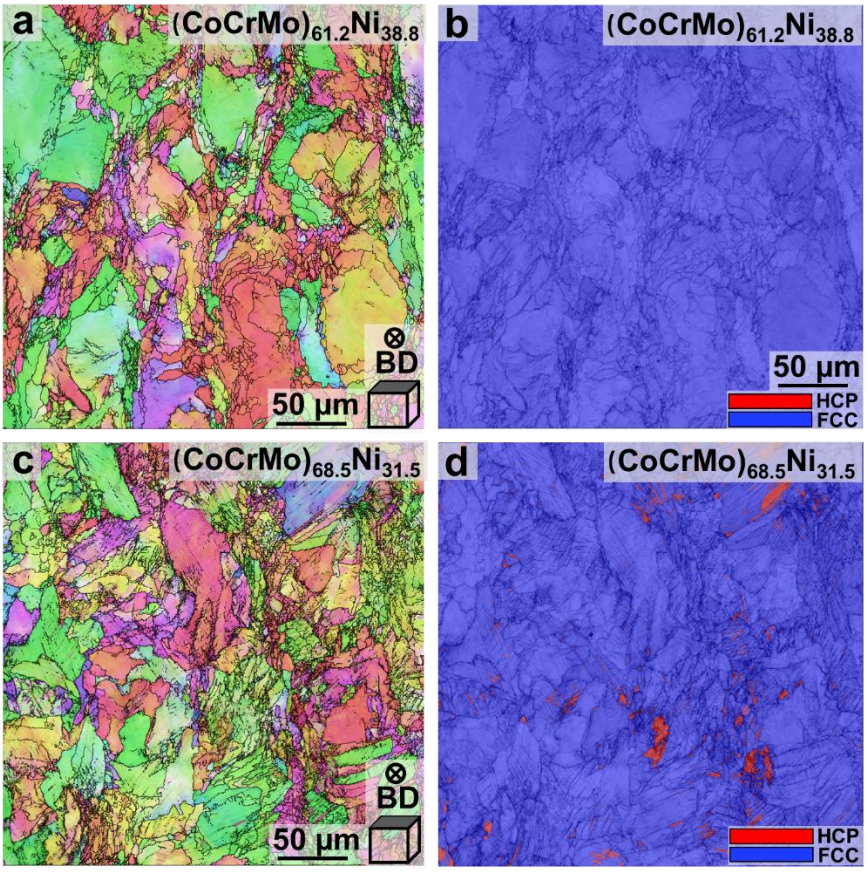

Figure 11. Orientation and phase maps of samples $(CoCrMo)_{61.2}Ni_{38.8}$ (a–b) and $(CoCrMo)_{68.5}Ni_{31.5}$ (c–d) tensile samples that are deformed for 10% engineering strain.

4.3. Insights from the in situ alloying induced chemical heterogeneities

Compared to *in situ* alloying, using pre-alloyed powders during LPBF typically results in relatively well-defined microstructural characteristics, i.e., mesostructures that are reminiscent of the scanning strategies and cellular structures (in some alloys). Tailoring such

features is relatively straightforward and has been proven to be effective in tuning the mechanical properties of the fabricated parts [57-60]. For instance, one of the most widely-explored methods is to modulate the size of cellular structures and then the mechanical performance of materials [34,61,62]. Furthermore, it is understood that the difference in thermal condition between the interior and boundary of the melt pool can result in various sizes of cellular structures [59] and grains [60]. However, appreciation for the potential of *in situ* alloying for modulating the meso-/micro-structures for enhancing the mechanical performance of the metallic parts started only recently [6,7]. Due to the complexity (especially the differences in the physical properties of multiple powders) of *in situ* alloying, precise control of the resultant microstructures is difficult (as compared to using pre-alloyed powders). Hence, it is more often used for the purposes of compositional design and rapid verification of unexplored alloys. Nevertheless, as illustrated through the present work, the unique features of *in situ* alloying (e.g., microscale chemical segregation) can in fact be potentially modulated to form desirable patterns (e.g., banded chemical distributions) to achieve superior mechanical property combinations.

Needless to say, this work, while highlighting the promise of tuning the chemical heterogeneities for enhanced performance, can only be considered preliminary (in terms of the potential that *in situ* alloying during AM has to offer). Therefore, the following are some of the promising aspects that need to be further pursued. (i) The volume fraction, morphology, and relative hardness values of chemical segregations can be tailored (via modulating the powder mixing duration, relationship between melt pool depth and layer thickness, SFEs of the components, properties of the minor powders, etc.) to explore the conditions that can achieve desirable mechanical performance. Similar principles already exist for designing the metal-matrix composites, where the characteristics of the reinforcement play significant roles in the mechanical properties [63]. Adapting some of those principles for *in situ* alloying using LPBF might lead to interesting results and may open new avenues for alloy design that exploits some of the intrinsic features of AM. (ii) The length scale of the chemically heterogeneous bands and the thickness ratio between them can be manipulated. For example, different scanning rotation angles (in addition to 67º) can result in varying levels of scan direction repetition and thus the thicknesses of bands. (iii) Other patterned chemical distributions could also be pursued, e.g., gradient along BD or core-shell structure, and their effect on the mechanical properties of the parts can be examined and/or compared. Furthermore, by altering scanning strategy during the printing process at varying locations/build heights, more versatility to the heterogeneous mesostructures may be

accomplished, which could potentially lead to even better mechanical properties and/or other interesting phenomena. (iv) The applicability and effect of this method to a wide range of materials systems can be examined. For example, instead of the single FCC phase that is presented in the current study, dual phase alloy system can be explored, where the chemical heterogeneity patterns may act as the templates for phase transformation during fabrication or upon post processing. A relevant approach has been successfully utilized in conventionally manufactured steels [64].

5. Summary

A compositionally graded CoCrMo-Ni alloy, with the Ni content ranging from ~26.8 to 98.8 at.%, was fabricated using the LPBF process, and the gradations in the microstructure, mechanical properties, and distributions of chemical heterogeneities (Co- and Ni-ribbons) in it were examined in detail. The novel findings in this work are summarized as follows.

1) Throughout the graded alloy coupon, chemically segregated bands are observed in samples with the average Ni content ranging from 92.2 to 26.8 at.%, which is a result of the incomplete mixing of the powders and 67° scan rotation. More specifically, chemical heterogeneities originate from the limited mixing time during fabrication while the continuous scan rotation affects their distribution in each layer, and eventually results in banded pattern with alternating homogeneous and heterogeneous bands.
2) Micro- and nano-indentation characterizations revealed that the presence of Co- and Ni-rich ribbon-like microstructural features significantly affect the local mechanical properties of the alloy. While the Co-ribbons result in hardening and Ni-ribbons cause softening. Statistical analysis on the micro-scratch test results shows that the banded pattern of chemical heterogeneities leads to the bimodal distribution of local hardness in the samples with the overall compositions ranging from $(CoCrMo)_{7.8}Ni_{92.2}$ to $(CoCrMo)_{61.2}Ni_{38.8}$. Additional hard peaks in the probability density function plots were observed in $(CoCrMo)_{63.3}Ni_{36.7}$, $(CoCrMo)_{68.5}Ni_{31.5}$, and $(CoCrMo)_{73.2}Ni_{26.8}$ samples.
3) Co- and Ni-ribbons have distinct SFEs and favor different deformation mechanisms. Low SFE (negative) in Co-ribbons leads to dissociation of full dislocations and planar slip of partials; relatively high SFE in Ni-ribbons favors cross-slip of screw dislocations and ‘homogenization’ of plastic deformation. The strain partitioning

between ribbon-ribbon or ribbon-matrix results in the generation of back stress or kinematic hardening.

4) Post-mortem EBSD characterization on the tensile and scratched samples confirmed that the superior properties of $(CoCrMo)_{63.3}Ni_{36.7}$, $(CoCrMo)_{68.5}Ni_{31.5}$, and $(CoCrMo)_{73.2}Ni_{26.8}$ samples are attributed to the strain-induced martensitic transformation. The Co-ribbons in these samples can reach critical SFE that makes the as-printed FCC phase metastable. Further plastic strain will trigger martensitic transformation and yield significant work hardening ability.

Our work highlights the possibility of modulating the chemical segregations that form during *in situ* alloying and their critical role in simultaneously enhancing the strength and strain-hardening ability (via kinematic strengthening) in AM alloys.

Acknowledgement

This work was supported by Agency for Science, Technology and Research (A*STAR) of Singapore via the Structural Metal Alloys Programme (No. A18B1b0061).

Data availability

The data that support the findings of this study are available from the corresponding author on reasonable request.

References

[1] T. DebRoy, H. L. Wei, J. S. Zuback, T. Mukherjee, J. W. Elmer, J. O. Milewski, A. M. Beese, A. Wilson-Heid, A. De, W. Zhang, Additive manufacturing of metallic components – Process, structure and properties, Progress in Materials Science 92 (2018) 112-224.
[2] T. H. Becker, P. Kumar, U. Ramamurty, Fracture and fatigue in additively manufactured metals, Acta Materialia 219 (2021) 117240.
[3] Z. Zhu, X. An, W. Lu, Z. Li, F. L. Ng, X. Liao, U. Ramamurty, S. M. L. Nai, J. Wei, Selective laser melting enabling the hierarchically heterogeneous microstructure and excellent mechanical properties in an interstitial solute strengthened high entropy alloy, Materials Research Letters 7 (2019) 453-459.
[4] S. Wei, C. Hutchinson, U. Ramamurty, Mesostructure engineering in additive manufacturing of alloys, Scripta Materialia 230 (2023) 115429.
[5] S. G. Jeong, G. M. Karthik, E. S. Kim, A. Zargaran, S. Y. Ahn, M. J. Sagong, S. H. Kang, J.-W. Cho, H. S. Kim, Architectured heterogeneous alloys with selective laser melting, Scripta Materialia 208 (2022) 114332.

[6] T. Zhang, Z. Huang, T. Yang, H. Kong, J. Luan, A. Wang, D. Wang, W. Kuo, Y. Wang, C.-T. Liu, In situ design of advanced titanium alloy with concentration modulations by additive manufacturing, Science 374 (2021) 478-482.
[7] H. Li, S. Thomas, C. Hutchinson, Delivering microstructural complexity to additively manufactured metals through controlled mesoscale chemical heterogeneity, Acta Materialia 226 (2022) 117637.
[8] S.-H. Li, Y. Zhao, J. Radhakrishnan, U. Ramamurty, A micropillar compression investigation into the plastic flow properties of additively manufactured alloys, Acta Materialia 240 (2022) 118290.
[9] K. M. Bertsch, G. Meric de Bellefon, B. Kuehl, D. J. Thoma, Origin of dislocation structures in an additively manufactured austenitic stainless steel 316L, Acta Materialia 199 (2020) 19-33.
[10] S. L. Sing, S. Huang, G. D. Goh, G. L. Goh, C. F. Tey, J. H. K. Tan, W. Y. Yeong, Emerging metallic systems for additive manufacturing: In-situ alloying and multi-metal processing in laser powder bed fusion, Progress in Materials Science 119 (2021) 100795.
[11] M. Simonelli, N. T. Aboulkhair, P. Cohen, J. W. Murray, A. T. Clare, C. Tuck, R. J. M. Hague, A comparison of Ti-6Al-4V in-situ alloying in Selective Laser Melting using simply-mixed and satellited powder blend feedstocks, Materials Characterization 143 (2018) 118-126.
[12] S. Huang, P. Kumar, W. Y. Yeong, R. L. Narayan, U. Ramamurty, Fracture behavior of laser powder bed fusion fabricated Ti41Nb via in-situ alloying, Acta Materialia 225 (2022) 117593.
[13] J. H. Martin, B. D. Yahata, J. M. Hundley, J. A. Mayer, T. A. Schaedler, T. M. Pollock, 3D printing of high-strength aluminium alloys, Nature 549 (2017) 365-369.
[14] S. Huang, R. L. Narayan, J. H. K. Tan, S. L. Sing, W. Y. Yeong, Resolving the porosity-unmelted inclusion dilemma during in-situ alloying of Ti34Nb via laser powder bed fusion, Acta Materialia 204 (2021) 116522.
[15] A. Zafari, K. Xia, Superior titanium from hybridised microstructures – A new strategy for future alloys, Scripta Materialia 173 (2019) 61-65.
[16] Z. Liu, M. A. Meyers, Z. Zhang, R. O. Ritchie, Functional gradients and heterogeneities in biological materials: Design principles, functions, and bioinspired applications, Progress in materials science 88 (2017) 467-498.
[17] X. Li, L. Lu, J. Li, X. Zhang, H. Gao, Mechanical properties and deformation mechanisms of gradient nanostructured metals and alloys, Nature Reviews Materials 5 (2020) 706-723.
[18] Y. Zhu, X. Wu, Perspective on hetero-deformation induced (HDI) hardening and back stress, Materials Research Letters 7 (2019) 393-398.
[19] M. Yang, Y. Pan, F. Yuan, Y. Zhu, X. Wu, Back stress strengthening and strain hardening in gradient structure, Materials Research Letters 4 (2016) 145-151.
[20] X. Wu, M. Yang, F. Yuan, G. Wu, Y. Wei, X. Huang, Y. Zhu, Heterogeneous lamella structure unites ultrafine-grain strength with coarse-grain ductility, Proceedings of the National Academy of Sciences 112 (2015) 14501-14505.
[21] T. J. Fleming, A. Kavanagh, G. Duggan, The effect of melt temperature on the mechanical properties of cast ASTM F75 CoCrMo alloy as explained by nitrogen and oxygen content, Journal of Materials Research and Technology 9 (2020) 9479-9486.
[22] D. Errandonea, High-pressure melting curves of the transition metals Cu, Ni, Pd, and Pt, Physical Review B 87 (2013) 054108.
[23] B.-S. Lee, Y. Koizumi, H. Matsumoto, A. Chiba, Collective behavior of strain-induced martensitic transformation (SIMT) in biomedical Co–Cr–Mo–N alloy polycrystal: An ex-situ

electron backscattering diffraction study, Materials Science and Engineering: A 611 (2014) 263-273.
[24] A. Howie, P. R. Swann, Direct measurements of stacking-fault energies from observations of dislocation nodes, The Philosophical Magazine: A Journal of Theoretical Experimental and Applied Physics 6 (1961) 1215-1226.
[25] C. Song, M. Zhang, Y. Yang, D. Wang, Y. Jia-kuo, Morphology and properties of CoCrMo parts fabricated by selective laser melting, Materials Science and Engineering: A 713 (2018) 206-213.
[26] C. C. Clickner, J. W. Ekin, N. Cheggour, C. L. H. Thieme, Y. Qiao, Y. Y. Xie, A. Goyal, Mechanical properties of pure Ni and Ni-alloy substrate materials for Y–Ba–Cu–O coated superconductors, Cryogenics 46 (2006) 432-438.
[27] Y. Wen, B. Zhang, R. L. Narayan, P. Wang, X. Song, H. Zhao, U. Ramamurty, X. Qu, Laser powder bed fusion of compositionally graded CoCrMo-Inconel 718, Additive Manufacturing 40 (2021) 101926.
[28] C. Guo, S. Wei, Z. Wu, P. Wang, B. Zhang, U. Ramamurty, X. Qu, Effect of dual phase structure induced by chemical segregation on hot tearing reduction in additive manufacturing, Materials & Design 228 (2023) 111847.
[29] Y. Zhao, J.-M. Park, J.-i. Jang, U. Ramamurty, Bimodality of incipient plastic strength in face-centered cubic high-entropy alloys, Acta Materialia 202 (2021) 124-134.
[30] S. Wei, Y. Zhao, J.-i. Jang, U. Ramamurty, Rate-dependent mechanical behavior of single-, bi-, twinned-, and poly-crystals of CoCrFeNi high-entropy alloy, Journal of Materials Science & Technology 120 (2022) 253-264.
[31] W. H. Liu, Z. P. Lu, J. Y. He, J. H. Luan, Z. J. Wang, B. Liu, Y. Liu, M. W. Chen, C. T. Liu, Ductile CoCrFeNiMox high entropy alloys strengthened by hard intermetallic phases, Acta Materialia 116 (2016) 332-342.
[32] W. D. Nix, H. Gao, Indentation size effects in crystalline materials: A law for strain gradient plasticity, Journal of the Mechanics and Physics of Solids 46 (1998) 411-425.
[33] S. Wei, P. Kumar, K. B. Lau, D. Wuu, L.-L. Liew, F. Wei, S. L. Teo, A. Cheong, C. K. Ng, B. Zhang, C. C. Tan, P. Wang, U. Ramamurty, Effect of heat treatment on the microstructure and mechanical properties of 2.4 GPa grade maraging steel fabricated by laser powder bed fusion, Additive Manufacturing 59 (2022) 103190.
[34] D. Kong, C. Dong, S. Wei, X. Ni, L. Zhang, R. Li, L. Wang, C. Man, X. Li, About metastable cellular structure in additively manufactured austenitic stainless steels, Additive Manufacturing 38 (2021) 101804.
[35] F. Wei, S. Wei, K. B. Lau, W. H. Teh, J. J. Lee, H. L. Seng, C. C. Tan, P. Wang, U. Ramamurty, Compositionally graded AlxCoCrFeNi high-entropy alloy manufactured by laser powder bed fusion, Materialia 21 (2022) 101308.
[36] S. Wei, K. B. Lau, J. J. Lee, F. Wei, W. H. Teh, B. Zhang, C. C. Tan, P. Wang, U. Ramamurty, Selective laser melting of Fe–Al alloys with simultaneous gradients in composition and microstructure, Materials Science and Engineering: A 821 (2021) 141608.
[37] J. M. Skelton, E. J. Sullivan, J. M. Fitz-Gerald, J. A. Floro, Efficacy of elemental mixing of in situ alloyed Al-33wt%Cu during laser powder bed fusion, Journal of Materials Processing Technology 299 (2022) 117379.
[38] L. Yao, S. Huang, U. Ramamurty, Z. Xiao, On the formation of “Fish-scale” morphology with curved grain interfacial microstructures during selective laser melting of dissimilar alloys, Acta Materialia 220 (2021) 117331.
[39] P. Kumar, O. Prakash, U. Ramamurty, Micro-and meso-structures and their influence on mechanical properties of selectively laser melted Ti-6Al-4V, Acta Materialia 154 (2018) 246-260.

[40] N. Nadammal, T. Mishurova, T. Fritsch, I. Serrano-Munoz, A. Kromm, C. Haberland, P. D. Portella, G. Bruno, Critical role of scan strategies on the development of microstructure, texture, and residual stresses during laser powder bed fusion additive manufacturing, Additive Manufacturing 38 (2021) 101792.
[41] S. Wei, S. Zheng, L. Zhang, Y. Liu, J. Wang, Role of interfacial transition zones in the fracture of Cu/V nanolamellar multilayers, Materials Research Letters 8 (2020) 299-306.
[42] K. Lu, Making strong nanomaterials ductile with gradients, Science 345 (2014) 1455-1456.
[43] Z. Li, K. G. Pradeep, Y. Deng, D. Raabe, C. C. Tasan, Metastable high-entropy dual-phase alloys overcome the strength–ductility trade-off, Nature 534 (2016) 227-230.
[44] L. M. Brown, W. M. Stobbs, The work-hardening of copper-silica I. A model based on internal stresses, with no plastic relaxation, Philosophical Magazine 23 (1971) 1185-1199.
[45] J. da Costa Teixeira, L. Bourgeois, C. W. Sinclair, C. R. Hutchinson, The effect of shear-resistant, plate-shaped precipitates on the work hardening of Al alloys: Towards a prediction of the strength–elongation correlation, Acta Materialia 57 (2009) 6075-6089.
[46] D. T. Pierce, J. A. Jiménez, J. Bentley, D. Raabe, J. E. Wittig, The influence of stacking fault energy on the microstructural and strain-hardening evolution of Fe–Mn–Al–Si steels during tensile deformation, Acta Materialia 100 (2015) 178-190.
[47] R. Stoltz, J. Vander Sande, The effect of nitrogen on stacking fault energy of Fe-Ni-Cr-Mn steels, Metallurgical Transactions A 11 (1980) 1033-1037.
[48] R. Reed, R. Schramm, Relationship between stacking - fault energy and x - ray measurements of stacking - fault probability and microstrain, Journal of Applied Physics 45 (1974) 4705-4711.
[49] J. Unfried-Silgado, L. Wu, F. Furlan Ferreira, C. Mario Garzón, A. J. Ramírez, Stacking fault energy measurements in solid solution strengthened Ni–Cr–Fe alloys using synchrotron radiation, Materials Science and Engineering: A 558 (2012) 70-75.
[50] T. L. Achmad, W. Fu, H. Chen, C. Zhang, Z.-G. Yang, First-principles calculations of generalized-stacking-fault-energy of Co-based alloys, Computational Materials Science 121 (2016) 86-96.
[51] L.-Y. Tian, R. Lizárraga, H. Larsson, E. Holmström, L. Vitos, A first principles study of the stacking fault energies for fcc Co-based binary alloys, Acta Materialia 136 (2017) 215-223.
[52] Z.-S. Wang, Y.-J. Guan, G.-C. Wang, C.-K. Zhong, Influences of die structure on constrained groove pressing of commercially pure Ni sheets, Journal of Materials Processing Technology 215 (2015) 205-218.
[53] Y. Koizumi, S. Suzuki, K. Yamanaka, B.-S. Lee, K. Sato, Y. Li, S. Kurosu, H. Matsumoto, A. Chiba, Strain-induced martensitic transformation near twin boundaries in a biomedical Co–Cr–Mo alloy with negative stacking fault energy, Acta Materialia 61 (2013) 1648-1661.
[54] K. Yamanaka, M. Mori, S. Kurosu, H. Matsumoto, A. Chiba, Ultrafine grain refinement of biomedical Co-29Cr-6Mo alloy during conventional hot-compression deformation, Metallurgical and materials transactions A 40 (2009) 1980-1994.
[55] S. Shang, W. Wang, Y. Wang, Y. Du, J. Zhang, A. Patel, Z. Liu, Temperature-dependent ideal strength and stacking fault energy of fcc Ni: a first-principles study of shear deformation, Journal of Physics: Condensed Matter 24 (2012) 155402.
[56] L. Remy, A. Pineau, Twinning and strain-induced FCC→ HCP transformation in the FeMnCrC system, Materials Science and Engineering 28 (1977) 99-107.
[57] L. Liu, Q. Ding, Y. Zhong, J. Zou, J. Wu, Y.-L. Chiu, J. Li, Z. Zhang, Q. Yu, Z. Shen, Dislocation network in additive manufactured steel breaks strength–ductility trade-off, Materials Today 21 (2018) 354-361.

[58] P. Kumar, R. Jayaraj, J. Suryawanshi, U. R. Satwik, J. McKinnell, U. Ramamurty, Fatigue strength of additively manufactured 316L austenitic stainless steel, Acta Materialia 199 (2020) 225-239.
[59] J. Suryawanshi, K. G. Prashanth, S. Scudino, J. Eckert, O. Prakash, U. Ramamurty, Simultaneous enhancements of strength and toughness in an Al-12Si alloy synthesized using selective laser melting, Acta Materialia 115 (2016) 285-294.
[60] P. He, R. F. Webster, V. Yakubov, H. Kong, Q. Yang, S. Huang, M. Ferry, J. J. Kruzic, X. Li, Fatigue and dynamic aging behavior of a high strength Al-5024 alloy fabricated by laser powder bed fusion additive manufacturing, Acta Materialia 220 (2021) 117312.
[61] D. Kong, C. Dong, X. Ni, L. Zhang, X. Li, Cellular size dependence on the strength of additively manufactured austenitic stainless steel, Materials Letters 279 (2020) 128524.
[62] Z. Li, B. He, Q. Guo, Strengthening and hardening mechanisms of additively manufactured stainless steels: The role of cell sizes, Scripta Materialia 177 (2020) 17-21.
[63] L. J. Huang, L. Geng, H. X. Peng, Microstructurally inhomogeneous composites: Is a homogeneous reinforcement distribution optimal?, Progress in materials science 71 (2015) 93-168.
[64] W. Sun, Y. Wu, S. Yang, C. Hutchinson, Advanced high strength steel (AHSS) development through chemical patterning of austenite, Scripta Materailia 146 (2018) 60-63.